Structural and photoluminescence properties of Eu³⁺ doped α-Ag₂WO₄ synthesized by the green coprecipitation methodology†

Ivo M. Pinatti,[a] Içamira C. Nogueira,[b] Wyllamanney S. Pereira,[a] Paula F. S. Pereira,[c] Rosana F. Gonçalves,[d] José A. Varela,[c] Elson Longo[c] and Ieda L. V. Rosa*[a]

Europium doped silver tungstates α-Ag$_{2-3x}$Eu$_x$WO$_4$ (x = 0, 0.0025, 0.005, 0.0075 and 0.01 mol) were synthesized by the coprecipitation method at 90 °C for 30 minutes. These crystals were structurally characterized by means of X-ray diffraction (XRD), Rietveld refinement, and micro-Raman (MR) and Fourier transformed infrared (FT-IR) spectroscopies. Field emission scanning electron microscopy (FE-SEM) images were employed to observe the shape of the crystals. The optical properties were investigated by ultraviolet-visible (UV-vis) absorption and photoluminescence (PL) measurements. The XRD pattern indicated structural organization at a long range for all undoped and Eu-doped samples, while MR and FT-IR revealed that the presence of the Eu³⁺ ions favors the structural organization at a short range. The Rietveld refinement showed that all the crystals are monophasic with an orthorhombic structure and the $Pn\bar{2}n$ space group. The refined lattice parameters and atomic positions were employed to model the WO$_6$ and AgO$_n$ (n = 2, 4, 6 and 7) polyhedra in the unit cell. FE-SEM analysis revealed nanorod-like microcrystals with growth of metallic silver on the surface. Further, the UV-vis absorption spectra indicated the existence of intermediary energy levels within the band gap. PL spectra showed a broad band related to the [WO$_6$] group and characteristic narrow peaks due to the f–f transitions of Eu³⁺ as a result of efficient energy transfer from the matrix. Also, the emission line shape transitions from ⁵D₀ to ⁷F$_J$ (J = 0–4) levels of the Eu³⁺ were noticed. Among the samples, the most intense photoluminescence results were observed for the α-Ag$_{2-3x}$Eu$_x$WO$_4$ (x = 0.0075) sample. Lifetime decays support that the Eu³⁺ ions occupy at least two crystallographic sites. CIE coordinates confirmed the colors of the emission spectra which classify this material as a potential phosphor in the visible range.

Introduction

Eu³⁺ doped materials have attracted great interest in the science and technology field due to their use as intrinsic probes because of their non-degenerate ground state ⁷F₀ and non-overlapping $^{2S+1}L_J$ multiplets. This ion is sensitive to the local lattice symmetry and as a consequence it can be used to map out changes in the chemical environment. These advantages arise from its special electronic configuration ([Xe]4f⁶) which also results in a pure and bright luminescence in the red region when excited in the ultraviolet (UV) electromagnetic range. As a consequence, Eu³⁺ doped materials are interesting for use as phosphors in displays, lasers, bio-medicine, magnets and other optoelectronic nanodevices.[1–3]

Silver tungstate (α-Ag₂WO₄) has emerged as a potential material in the class of metal tungstates with great applications including chemical fixation of CO₂,[4] as a catalyst in organic chemistry,[5] as a microbial agent,[6] as photoswitches,[7] in photoluminescence,[8] in photocatalysis of organic pollutants,[9–13] as lubricants,[14] in electrocatalysis,[15] as a novel ozone gas sensor[16] and as antimicrobial and antibacterial agents.[17] In addition, α-Ag₂WO₄ has also been studied because of the direct *in situ* observation of Ag growth on its surface when it is bombarded by an accelerated electron beam from an electron microscope under high vacuum.[18–21] Recently, Zhang *et al.*[22] synthesized silver tungstate with good visible light photocatalytic performance and antimicrobial activity for the hexagonal-phase of Ag₂WO₄.

ᵃINCTMN, LIEC, Chemistry Department of the Federal University of São Carlos, P.O. Box 676, 13565-905 São Carlos, SP, Brazil. E-mail: ilvrosa@ufscar.br; Fax: +55-16-33518208; Tel: +55-16-33518214
ᵇIFMA (Instituto Federal de Educação), Ciência e Tecnologia do Maranhão, PPGEM, São Luís, MA, Brazil
ᶜINCTMN, LIEC, Chemistry Institute of the State University of São Paulo, UNESP, P.O. Box 355, 14800-900 Araraquara, SP, Brazil
ᵈUNIFESP, Federal University of São Paulo, Rua Prof. Artur Riedel, 275, SP, 09972-270 Diadema, SP, Brazil

Direct excitation of Eu^{3+} ions is a relatively inefficient process due to the forbidden character of the 4f transitions, but Eu-doped inorganic materials can exhibit efficient luminescence emissions upon ultraviolet (UV) excitation. These materials have all the advantages of a large Stokes shift, a sharp emission spectrum, a long lifetime, high chemical/photochemical stability, low toxicity, and reduced photobleaching as a result of the shielding of the 4f electrons.[23] The rare earth ion Eu^{3+} has already been used to enhance the luminescence or intrinsic properties of various tungstate matrices.[24–31] These studies focused on the Eu^{3+} content to obtain the maximum PL intensity, especially for those associated with the $^5D_0 \rightarrow {}^7F_2$ transitions. Also, to study the Eu^{3+} influence on structural, optical and morphological behavior of these materials. A tungstate host lattice can act as a good matrix for rare earth ions as a consequence of their high thermal, physical and chemical stability, good absorption coefficient and high refraction index, which permits efficient energy transfer from the lattice to the activator ion. Moreover, tungstates have high luminescence intensity under UV and X-ray excitations due to their tetrahedron polyhedra (WO_6) which increases the possibility of obtaining new phosphors in the visible range. On the other hand, low luminescence efficiency appears to be a limitation for direct application of these materials. Consequently, there is a significant interest to increase the Eu^{3+} emission intensity and develop new europium doped tungstates for potential applications in many technological fields.

Luminescence intensity is directly correlated to shape and size distribution of the particles. In order to have appropriate morphological aspects, various synthetic routes have been used to produce silver tungstate including sonochemistry,[8] supersonic-assisted homogeneous precipitation,[17] conventional hydrothermal[9,32,33] and hydrothermal microwave.[6] Apparently, most of the aforementioned experimental procedures can be expensive, time consuming and need high temperature or pressure. In addition, these techniques can induce the agglomeration of the particles and clustering of the optically active lanthanide ions reducing their luminescence intensities. So, it is necessary to overcome these drawbacks with the use of mild-conditions for synthesis. Among the methods that have been put forward, coprecipitation appears to be an easy one to perform, and requires neither multisequential steps nor sophisticated equipment. This approach is also ecofriendly (water as solvent), cheaper, does not need high temperature or pressure, is industrially favorable, as well as yields materials with homogeneous shape and size without deleterious phases. Furthermore, it is not time-consuming and can be easily performed on a large scale by simple precipitation of the salt precursors.[34,35]
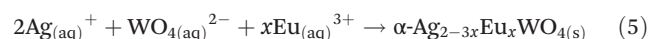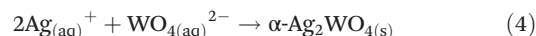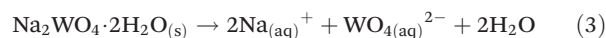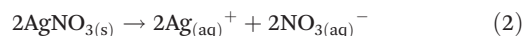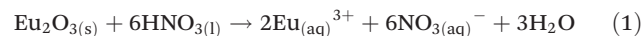
To the best of our knowledge, there are no photoluminescence studies related to the rare earth doping of silver tungstate using any kind of methodology. For this reason, the overall objective of this project is to study the structural and luminescence properties of undoped and Eu-doped silver tungstate. Different concentrations of Eu^{3+} in the silver tungstate host matrix were employed to determine the minimum concentration of this ion to promote changes in its structural and luminescence properties. The materials were obtained by the simple coprecipitation method at 90 °C for 30 minutes without further calcinations or treatments. X-ray diffraction, micro-Raman and Fourier transformed infrared were used for structural characterization. UV-vis and photoluminescence were employed as optical techniques to evaluate the local symmetry of Eu^{3+} in the matrix and FE-SEM was used to analyze both the shape and size of these crystals.

Experimental

Materials and methods

α-$Ag_{2-3x}Eu_xWO_4$ (x = 0, 0.0025, 0.005, 0.0075 and 0.01 mol) microcrystals were prepared by the coprecipitation (CP) method. In a typical experimental process, 1.0 mmol of sodium tungstate dihydrate ($Na_2WO_4 \cdot 2H_2O$ – 99%, Sigma-Aldrich) and 2.0 mmol of silver nitrate ($AgNO_3$ – 99.0%, Sigma-Aldrich) were dissolved separately in 50 mL of deionised water at 90 °C under magnetic stirring for 5 min. The Ag^+ solution was transferred into WO_4^{2-} solution and heated at 90 °C under constant stirring for 30 minutes. Instantaneously, a pale yellow suspension was formed with a temperature reduction to 70 °C. These crystals were obtained as a fine white powder precipitated at the bottom of the glass flask after turning off the stirring. After that, they were naturally cooled to room temperature, the precipitates were separated by centrifugation, washed with deionized water and acetone in sequence to remove any remaining sodium and nitrate ions. Finally, the crystals were collected and then dried in an oven at 60 °C for 12 h. The Eu-doped sample preparation follows the same procedure, except for the addition of appropriate amounts of Eu $(NO_3)_3$ solution into the Ag^+ solution. For the preparation of $Eu(NO_3)_3$ solution, europium oxide (Eu_2O_3 – 99.999%, Sigma-Aldrich) was precalcined at 900 °C for 2 h to achieve dehydration and decarbonation. Then it was prepared through the dissolution of Eu_2O_3 powder in a hot solution of dilute HNO_3 and heated until the excess acid had evaporated, and completed with H_2O, forming a 0.1 M solution of europium nitrate. The following equations refer to the procedure listed above.

$$Eu_2O_{3(s)} + 6HNO_{3(l)} \rightarrow 2Eu_{(aq)}^{3+} + 6NO_{3(aq)}^- + 3H_2O \quad (1)$$

$$2AgNO_{3(s)} \rightarrow 2Ag_{(aq)}^+ + 2NO_{3(aq)}^- \quad (2)$$

$$Na_2WO_4 \cdot 2H_2O_{(s)} \rightarrow 2Na_{(aq)}^+ + WO_{4(aq)}^{2-} + 2H_2O \quad (3)$$

$$2Ag_{(aq)}^+ + WO_{4(aq)}^{2-} \rightarrow \alpha\text{-}Ag_2WO_{4(s)} \quad (4)$$

$$2Ag_{(aq)}^+ + WO_{4(aq)}^{2-} + xEu_{(aq)}^{3+} \rightarrow \alpha\text{-}Ag_{2-3x}Eu_xWO_{4(s)} \quad (5)$$

Characterization

Powder X-ray diffraction (XRD) measurements were performed on a Rigaku-D/max 2500 diffractometer (Japan) with graphite-

monochromatized Cu Kα radiation (λ = 0.15405 nm). The scan was performed from 5° to 80° with a scanning velocity of 2° min^{-1}. Rietveld refinements of the measured XRD patterns from 5° to 110° with a scanning velocity of 1° min^{-1} were carried out using the general structure analysis (GSAS) program.[36] Micro-Raman (MR) scattering measurements were performed using a 632.81 nm line of an He–Ne laser as an excitation source. The spectra were recorded using a T-64000 (Jobin–Yvon) triple monochromator coupled to a CCD detector in the range of 25–1000 cm^{-1}. Fourier transform infrared (FT-IR) spectroscopy data were recorded on a Bomem–Michelson spectrophotometer using KBr pellets as a reference in the transmittance mode (model MB-102). The spectrum was recorded in the range of 250 to 1000 cm^{-1} with a resolution of 4 cm^{-1} and 32 times scanning. UV-visible diffuse reflectance spectroscopy (UV-vis) was performed on a UV-visible spectrometer (Varian, model Cary 5G) and the spectra were recorded in a diffuse-reflectance mode. Photoluminescence (PL) measurements were performed by using a Thermo Jarrell Ash monochromator (27 cm) coupled to a visible detector (photomultiplier PMT R955, Hamamatsu, 500 V – filter L37). A Kr$^+$ Innova 200 laser (Coherent, λ = 350.7 nm) was used as the excitation source. Its maximum output power was maintained at 500 mW. PL data of the Eu-doped powders were obtained using a Jobin Yvon – Fluorolog III spectrofluorometer under excitation of a 450 W xenon lamp. The luminescence lifetime measurements were carried out as well using a 1940D model spectrophosphorometer coupled to the spectrofluorometer. All the PL measurements were performed at room temperature. The shape and size of the crystals were observed by field emission scanning electron microscopy (FE-SEM) using a Carl Zeiss microscope (Model Supra 35) operated at an accelerating voltage of 30 kV and a working distance of 3.7 mm.

Fig. 1 (A) XRD of the α-Ag$_{2-3x}$Eu$_x$WO$_4$ synthesized by the coprecipitation method at 90 °C for 30 minutes. (B) Magnification of region between 29° and 34°. (a) x = 0, (b) x = 0.0025, (c) x = 0.005, (d) x = 0.0075 and (e) x = 0.01.

Results and discussion

X-ray diffraction (XRD)

Fig. 1(A) illustrates the diffraction pattern of the α-Ag$_{2-3x}$Eu$_x$WO$_4$ (x = 0, 0.0025, 0.005, 0.0075 and 0.01 mol) samples synthesized by the CP method at 90 °C for 30 minutes. The intense and well-defined peaks are related to the orthorhombic phase, non-centrosymmetric space group $Pn\bar{2}n$, point-group of symmetry C_{2v}^{10} and two molecular formulas per unit cell (Z = 2) of α-Ag$_2$WO$_4$. All the diffraction peaks are well accordant with Inorganic Crystal Structure Database (ICSD) no. 4165 pattern and indicates the phase purity of the samples.[37] The strong and clear peaks observed in Fig. 1 indicate the high crystallinity of the materials which also favors a bright luminescence.[2]

After analyzing this diffraction pattern, it can be concluded that the precursor was completely converted to α-Ag$_{2-3x}$Eu$_x$WO$_4$ (x = 0, 0.0025, 0.005, 0.0075 and 0.01 mol) with the time and temperature used. Once the secondary phase or phases related to precursors were not observed, it can be concluded that Eu^{3+} ions were incorporated into the lattice. Due
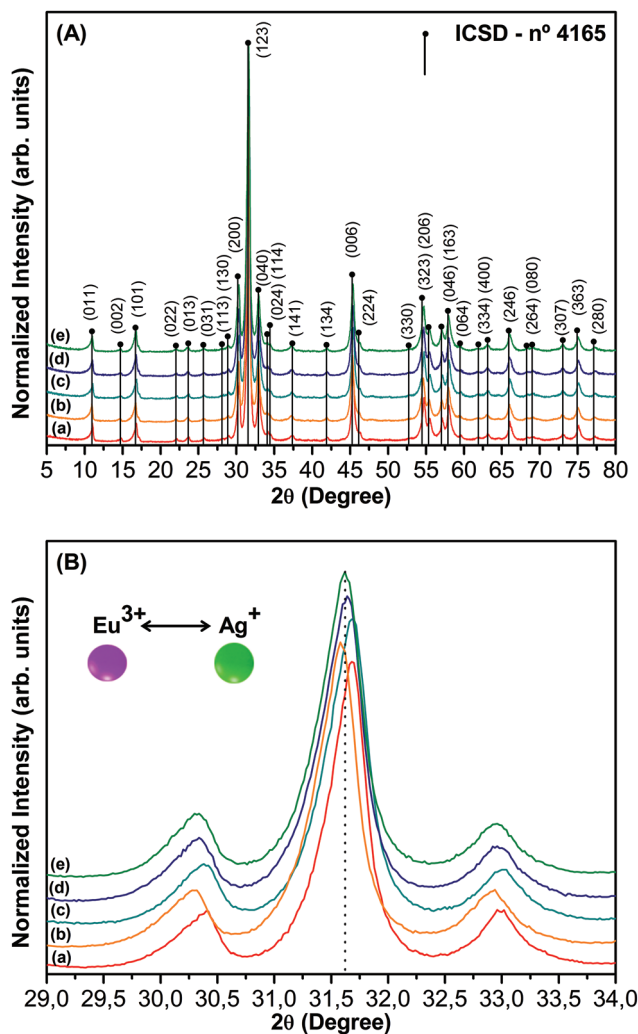
to different coordination numbers, ionic radii and electronic densities (charge) between W^{6+} (0.060 nm; coordination number = 4) and Eu^{3+} (0.125 nm; coordination number = 8), Eu^{3+} is expected to occupy the Ag$^+$ (0.115 nm) site in this crystal.

Fig. 1(B) shows a small shift in the strongest peak (123) position to a lower angle of the Eu-doped samples compared to undoped α-Ag$_2$WO$_4$. This is because the radius of Eu^{3+} is a little bigger than Ag$^+$, which results in a bigger crystal plane spacing d, according to Bragg's equation $n\lambda = 2d\sin\theta$ (where n = constant, λ is the wavelength of the X-ray and the θ is the angle). This behavior indicates that Eu^{3+} ions have been efficiently doped into the crystal lattice of α-Ag$_2$WO$_4$ and provoked slight expansion of the unit cell volume.[29,38] The crystalline phase was clearly observed for all doped samples and no phase transformation was observed with the dopant.[39] These

results show order at a long range and are accordant with the literature.[28,29]

Rietveld analysis

The Rietveld refinement method[40] was employed to understand whether there are differences in the structural arrangements of the undoped and Eu-doped samples. In these analyses, the refined parameters were the scale factor, background, shift lattice constants, profile half-width parameters (u, v, w), isotropic thermal parameters, lattice parameters, strain anisotropy factor, preferred orientation and atomic functional positions. The background was corrected using a Chebyshev polynomial of the first kind. The peak profile function was modeled using a convolution of the Thompson–Cox–Hastings pseudo-Voigt (pV-TCH)[41] with the asymmetry function described by Finger et al.,[42] which accounts for the asymmetry due to axial divergence. To account for the anisotropy in the half width of the reflections, the model by Stephens[43] was used. Rietveld refinement plots for the observed pattern versus calculated patterns of the α-$Ag_{2-3x}Eu_xWO_4$ (x = 0, 0.0025, 0.005, 0.0075 and 0.01 mol) are shown in Fig. SI1 (a–e).†

The measured diffraction patterns were well adjusted to the ICSD no. 4165.[37] The difference between XRD pattern profiles experimentally observed and the theoretically calculated data displays small differences near to zero in the intensity scale as illustrated by a line ($Y_{Obs} - Y_{Calc}$). More details about the quality of the structural refinement are displayed in Table SI1.† This table shows low deviations of statistical parameters (R_{wp}, R_p, R_{Bragg} and χ^2) which suggest that the refinement results are quite reliable and good numerical results. Structural refinement data confirm that all α-Ag_2WO_4 crystals are crystallized in an orthorhombic structure with a symmetry space group named for Hermann–Mauguin ($Pn\bar{2}n$) and two molecular formula per unit cell (Z = 2).[37] The experimental lattice parameters and unit cell volumes calculated using the Rietveld refinement method[40] are also shown in Table SI1.† A slight increase in the lattice parameter values is observed with the substitution of silver by europium atoms probably due to the replacement of [AgO_n] by [EuO_n] (n = 2, 4, 6 and 7) polyhedra which cause expansion in the electron density in the Ag site and increase in the cell volume of the orthorhombic structure.

It is interesting to note that there are some variations in the atomic positions related to the oxygen atoms (Tables SI2 and SI3†) while the other atoms practically keep their positions fixed within the structure. Therefore, we believe that these variations in the atomic positions of oxygen atoms can lead to distortions on the [WO_6], [AgO_n] and [EuO_n] (n = 2, 4, 6 and 7) polyhedra present in the structure of α-$Ag_{2-3x}Eu_xWO_4$ crystals.

Moreover, in Table SI1† the values of network parameters and cell volume obtained in this work are compared with those published in the literature. Small variations between these values were verified. This may be related to the peculiarity of each synthesis method where the experimental variables (temperature, processing time, heating rate, solvents, etc.) probably influence the organization of the [WO_6], [AgO_n]

and [EuO_n] (n = 2, 4, 6 and 7) polyhedra within the crystal lattice. Also, these variables cause the formation or reduction of structural defects (oxygen vacancies, distortion on the bonds, stresses and strains on the crystalline lattice) in the materials.

Unit cell representation

The schematic representation of unit cells of orthorhombic α-$Ag_{2-3x}Eu_xWO_4$ (x = 0.01 mol) microcrystals is illustrated in Fig. 2. This unit cell was modeled through the Visualization for Electronic and Structural Analysis (VESTA) program,[44] version 3 for Windows®. This unit cell was modeled using lattice parameters and atomic positions obtained from the Rietveld refinement data shown in Table SI1† for the α-$Ag_{2-3x}Eu_xWO_4$ (x = 0.01 mol) microcrystals obtained by the CP method.

Cavalcante et al.[8] studied pure α-Ag_2WO_4 and concluded the existence of distorted WO_6 polyhedra with octahedral configuration, these polyhedra consisting of three different W atoms, where all of them are coordinated to six O atoms. Otherwise, Ag atoms can have four types of coordinations: (i) Ag coordinated by seven O atoms (AgO_7 deltahedral polyhedra); (ii) Ag coordinated by six O atoms (AgO_6 octahedral polyhedra); (iii) Ag coordinated by four O atoms (AgO_4 tetrahedral polyhedra) and (iv) Ag coordinated by two O atoms (AgO_2 angular polyhedra). WO_6 and AgO_n (n = 2, 4, 6 and 7) polyhedra are distorted in the crystal lattice caused by difference in bond angles, which results in different order–disorder levels and/or distortions in the α-Ag_2WO_4 crystal lattice. In addition, the presence of Eu^{3+} can also influence these distortions, which are confirmed by XRD and Rietveld refinement analyses.

Micro-Raman spectroscopy (MR)

Micro-Raman (MR) spectroscopy is a powerful tool to analyze the configuration of ceramic materials. Through this technique it is possible to observe structural defects as well as the framework organization in the short range. Raman
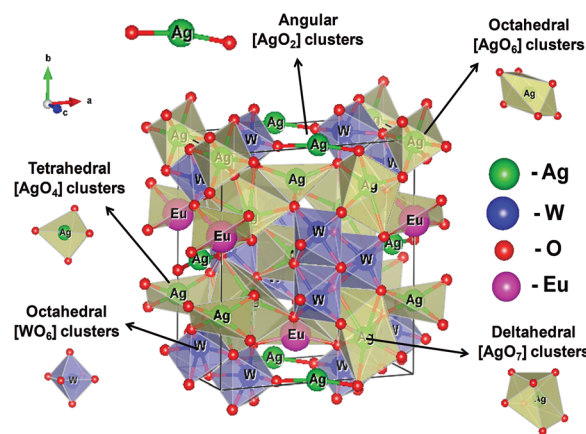

Fig. 2 Schematic representation of crystalline unit cells of α-$Ag_{2-3x}Eu_xWO_4$ (x = 0.01) microcrystals.
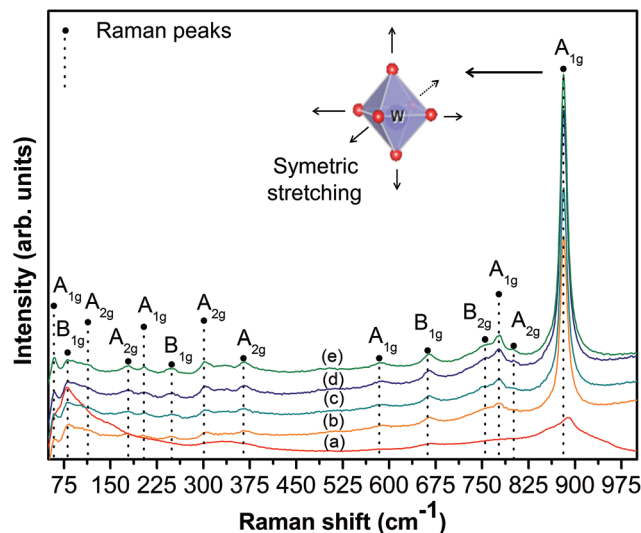
Fig. 3 MR of the α-Ag$_{2-3x}$Eu$_x$WO$_4$ synthesized by the coprecipitation method at 90 °C for 30 minutes. (a) $x = 0$, (b) $x = 0.0025$, (c) $x = 0.005$, (d) $x = 0.0075$ and (e) $x = 0.01$.

Table 1 Raman modes of α-Ag$_{2-3x}$Eu$_x$WO$_4$ (x = 0, 0.0025, 0.005, 0.0075 and 0.01 mol) synthesized by the coprecipitation method at 90 °C for 30 minutes compared to the literature

Symbol	Wavenumber (cm^{-1})		
	Turkovic[46]	Theoretical[19]	This work
A$_{1g}$	44	39	—
A$_{1g}$	60	57	59
B$_{1g}$	92	89	81
A$_{2g}$	116	—	114
	182	179	179
A$_{1g}$	208	204	204
B$_{1g}$	248	246	249
A$_{2g}$	306	302	301
B$_{2g}$	336	332	—
A$_{2g}$	366	363	365
B$_{2g}$	488	485	—
B$_{2g}$	510	504	—
	546	—	—
A$_{1g}$	590	578	584
B$_{1g}$	629	—	—
	667	661	662
	730	—	—
B$_{2g}$	754	757	755
A$_{1g}$	778	774	777
A$_{2g}$	800	799	801
A$_{1g}$	884	878	881

spectroscopy is based on the inelastic scattering of photons, which lose energy by exciting vibrations in the sample.

Fig. 3 represents MR spectra of the α-Ag$_{2-3x}$Eu$_x$WO$_4$ (x = 0, 0.0025, 0.005, 0.0075 and 0.01 mol) samples synthesized at 90 °C for 30 minutes. Vibrational modes detected in silver tungstate can be separated into two parts due to the weak coupling between the ionic group (WO$_4^{2-}$) and Ag$^+$: (i) external modes or lattice phonons, which are related to the motion of Ag$^+$; and (ii) internal modes, which are related to the oscillations inside the WO$_4^{2-}$ polyhedra (the mass center is in the stationary state).

WO$_4^{2-}$ tetrahedron in free space has point symmetry T_d which is reduced to tetragonal S_4 when it is placed into the structure. This results in the splitting of all degenerate vibrations due to the Crystal Field (CF) effect. Moreover the presence of two molecular groups in the primitive cell further alters the structure of the vibrational modes due to Davydov Splitting (DS).[45,46]

It is possible to see the presence of 14 Raman-active vibrational modes for our sample. The mode at 59 cm^{-1} is relative to motion of heavy Ag$^+$ ions (external or lattice phonons). This mode is intense and is not present in other tungstates such as CaWO$_4$, SrWO$_4$, BaWO$_4$ or ZnWO$_4$. On the other hand, the modes higher than 800 cm^{-1} correspond to symmetric W–O stretching, and usually are present in any tungstate.[46]

The intense peak at around 880 cm^{-1} is attributed to the bending modes of the Ag–O–W unit.[9] It is possible to see an increase in the intensity of this mode, which is related to Eu^{3+} substitution in the Ag$^+$ site, which in turn can change this bending mode. This substitution changes energy bonding and bonding length of AgO$_n$ (n = 2, 4, 6 and 7) polyhedra which directly interfere with the WO$_6$ polyhedra. So, as a consequence, we can see a better definition of other modes as the Eu^{3+} content increases up to 0.01 mol.

Despite the fact that the increase in Eu^{3+} concentration did not show disorder at a long range, MR analyses show that this ion facilitates the structural organization at a short range, possibly due to vacancies that are generated in the host matrix and eventually decreases the tensions in the material, which causes a relaxation of the crystal lattice resulting in a better definition of the Raman modes.[47] So, we may assume that Eu^{3+} causes a degree of short range order in the α-Ag$_2$WO$_4$ matrix and it was capable of modifying stretching, torsion and bending vibrational modes of the structure at a short range. These more intense and well defined peaks make this material suitable for use in lasers in Stimulated Raman Scattering (SRS).[45]

Table 1 lists a comparison of the modes obtained in this work related to silver tetratungstate obtained by Turkovic[46] and theoretical values obtained by Longo *et al.*[19] The theoretical Raman-active modes were calculated through the atomic positions and lattice parameters for the optimized α-Ag$_2$WO$_4$ crystals using first-principles calculation and did not consider the non-harmonic contribution to the crystal-lattice vibration phonons.

It is possible to detect some small variations of the Raman modes and some that have low intensity related to those reported in this work. These changes are a result of various interferences in the experimental procedure such as temperature, time and methodology. Other factors which also can influence Raman modes deviations are caused by crystal size and distortions of Ag–O bonds as a result of Eu^{3+} substitution in the Ag$^+$ site which can directly alter the motion of [AgO$_n$]–[WO$_6$]–[EuO$_n$] polyhedra. The changes in intensity are a result

of the rotation of the x-, y- and z-axes of the α-Ag$_2$WO$_4$ crystals which occurs at different scattering of the tensors and components.[46]

Fourier transformed infrared spectroscopy (FT-IR)

Fourier Transformed Infrared (FT-IR) spectroscopy was used to evaluate the degree of structural order–disorder in the metal–oxygen bonds. This is determined by the symmetry of the molecule and the functional groups presented. While Raman spectroscopy selection rule requires that the molecular polarizability changes during the vibration, infrared spectroscopy requires that the dipole moment of the molecule must change during the vibration for the absorption of a photon to occur. Fig. 4 represents the FT-IR spectra of the α-Ag$_{2-3x}$Eu$_x$WO$_4$ (x = 0, 0.0025, 0.005, 0.0075 and 0.01 mol) samples synthesized at 90 °C for 30 minutes in the range of 200–4000 cm^{-1}. This region comprises the mid-infrared where the molecular vibrations are detected.

In the spectra it is possible to see two intense absorptions at 817 and 859 cm^{-1} which are related to antisymmetric stretching vibrations of distorted [WO$_6$] polyhedra. The other two main bands occur at 313 and 362 cm^{-1} that represent external torsional motion and internal symmetric bending vibrations of distorted [WO$_6$] polyhedra, respectively. Vibrational frequencies are related to bond strength and mass of the vibrating atoms, which can split into more components as observed throughout the spectra of Eu-doped samples. This behavior is due to the influence of Eu^{3+} in some sites of Ag$^+$ which causes variation in the W–O stretching vibration.[48]

These results are in agreement with the theoretically calculated modes reported in the orthorhombic structure of α-Ag$_2$WO$_4$ microcrystals and MR spectra.[19,35,39,49] Some devi-
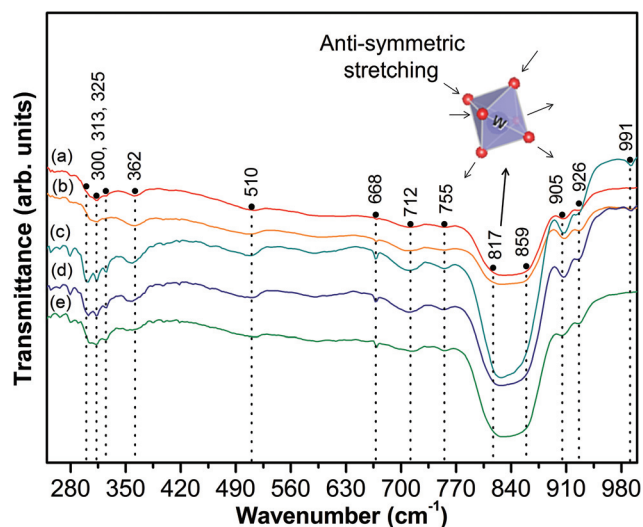
ations happen as a consequence of experimental conditions and especially by insertion of Eu^{3+} ions in the structure which modifies the interactions between AgO$_n$ (n = 2, 4, 6 and 7) and WO$_6$ polyhedra as explained by MR analysis. Altogether, micro-Raman and FT-IR spectroscopy indicate order at a short range with the increase of Eu^{3+} in the host matrix of α-Ag$_2$WO$_4$.

Diffused reflectance in ultraviolet visible spectroscopy (UV-vis)

In general, the optical absorption energy of the host lattice can be obtained by the diffuse reflectance spectra. Fig. 5(A) shows the UV-visible diffuse reflectance spectra of the α-Ag$_{2-3x}$-Eu$_x$WO$_4$ (x = 0, 0.0025, 0.005, 0.0075 and 0.01 mol) samples synthesized by the CP method at 90 °C for 30 minutes. It is possible to see a broad absorption band range from 250 to 400 nm for all samples, which is related to the electron transfer from the hybridized band of Ag 4d and O 2p to W 5d orbital. This defined absorption edge is related to the intrinsic transition of semiconductors and is not related to impurity levels.[2,12]

The electronic structure of the samples was verified through calculation of the band gap using the Kubelka & Munk-Aussig method.[50] This methodology is based on the transformation of diffuse reflectance measurements to esti-
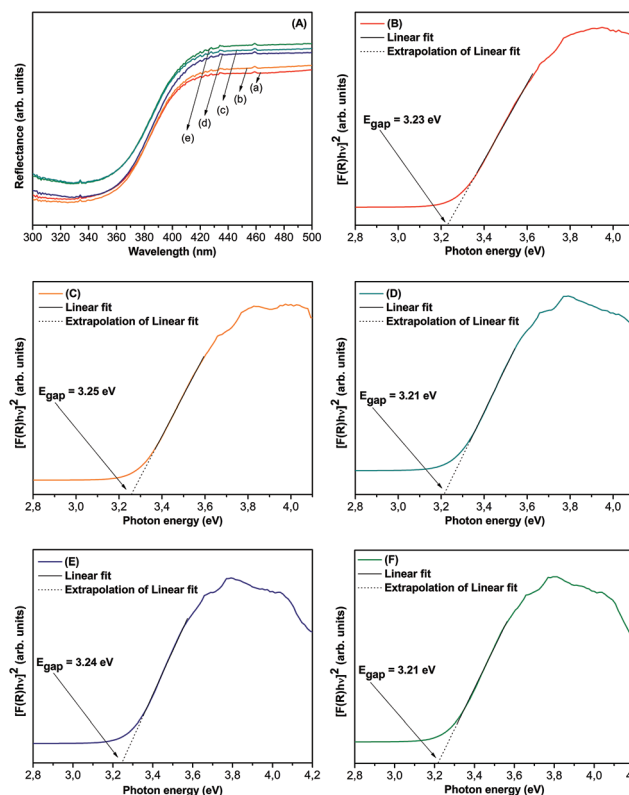
Fig. 5 (A) Diffuse reflectance spectra of the α-Ag$_{2-3x}$Eu$_x$WO$_4$ synthesized by the coprecipitation method at 90 °C for 30 minutes. (a) x = 0, (b) x = 0.0025, (c) x = 0.005, (d) x = 0.0075 and (e) x = 0.01. Absorbance of the samples (B) x = 0, (C) x = 0.0025, (D) x = 0.005, (E) x = 0.0075 and (F) x = 0.01.

Fig. 4 FT-IR of the α-Ag$_{2-3x}$Eu$_x$WO$_4$ synthesized by the coprecipitation method at 90 °C for 30 minutes. (a) x = 0, (b) x = 0.0025, (c) x = 0.005, (d) x = 0.0075 and (e) x = 0.01.

mate E_{gap} values with good accuracy within the limits of assumptions when modeled in three dimensions.[51]

It is particularly useful in limited cases of an infinitely thick sample layer. The Kubelka–Munk eqn (6) for any wavelength is described as

$$\frac{K}{S} = \frac{(1 - R_\infty)^2}{2R_\infty} = F(R_\infty) \qquad (6)$$

where $F(R_\infty)$ is the Kubelka–Munk function or absolute reflectance of the sample. Magnesium oxide (MgO) was the standard sample used in reflectance measurements. $R_\infty = R_{sample}/R_{MgO}$ (R is the reflectance when the sample is infinitely thick), k is the molar absorption coefficient and "s" is the scattering coefficient.

In a parabolic band structure, the optical band gap and absorption coefficient of semiconductor oxides[52] can be calculated by the following eqn (7):

$$\alpha h\nu = C_1(h\nu - E_{gap})^n \qquad (7)$$

where α is the linear absorption coefficient of the material, $h\nu$ is the photon energy, C_1 is a proportionality constant, E_{gap} is the optical band gap and n is a constant associated with different kinds of electronic transitions which for this material is $n = 1/2$ (direct allowed transitions[12,53]). Finally, using the remission function described in eqn (6) and with the term $k = 2\alpha$ and C_2 as a proportionality constant, we obtain the modified Kubelka–Munk eqn (8):

$$[F(R_\infty)h\nu]^2 = C_2(h\nu - E_{gap}) \qquad (8)$$

Therefore, plotting a graph of $[F(R_\infty)h\nu]^2$ against $h\nu$ and finding the value of $F(R_\infty)$, the E_{gap} values of the samples were determined, which is plotted in Fig. 5(B)–(F).

The band gaps of the samples were calculated as 3.23, 3.25, 3.21, 3.24 and 3.21 eV for α-Ag$_{2-3x}$Eu$_x$WO$_4$ ($x = 0$, 0.0025, 0.005, 0.0075 and 0.01 mol), respectively. The maximum energy gap value is related to the higher structure symmetry. The band gap energy values show deviations due to Eu^{3+} insertion. This is an evidence that the 4f orbitals of Eu^{3+} ions inserted in the matrix contributed to the creation of new intermediary energy levels in the region of the valence band (VB) and the conduction band (CB).[38] It is also known that the creation of intermediary levels in the band gap can be related to other factors such as particle shape, size, annealing temperature, processing time, preparation method and the kind of material (thin films or powders). Once these cited factors were maintained almost constant, little deviation on E_{gap} values is ascribed to the doping.

Photoluminescence (PL)

Fig. 6 shows the PL spectra recorded at room temperature of the α-Ag$_{2-3x}$Eu$_x$WO$_4$ ($x = 0$, 0.0025, 0.005, 0.0075 and 0.01 mol) samples excited by a 350.7 nm line of a krypton ion laser. In Fig. 6, a prominent band with maximum emission is clearly seen in the visible electromagnetic spectrum. It covers a broad range of wavelengths centered at 450 nm for all the samples
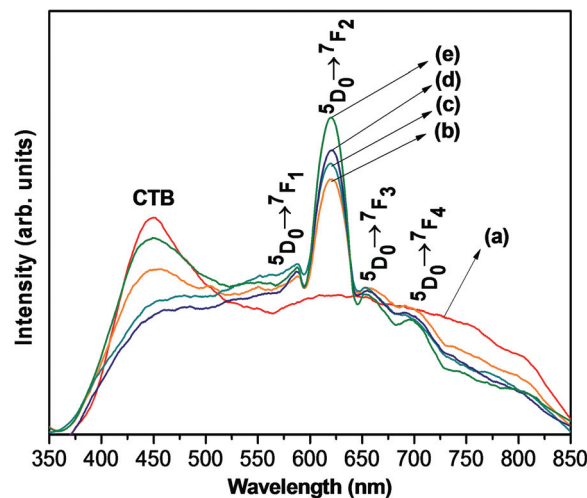

Fig. 6 Emission Spectra of the α-Ag$_{2-3x}$Eu$_x$WO$_4$ synthesized by the coprecipitation method at 90 °C for 30 minutes. (a) $x = 0$, (b) $x = 0.0025$, (c) $x = 0.005$, (d) $x = 0.0075$ and (e) $x = 0.01$.

and is related to the charge transfer band (CTB) within the [WO$_6$] polyhedra. In the red region there is also a small intensity broad band which is related to AgO$_n$ ($n = 2$, 4, 6 and 7) polyhedra.[19]

This PL behavior can be explained through complex polyhedra model based on Kröger–Vink notation.[54] It is well known that the concentration of different intrinsic (bulk/surface) and extrinsic (interface) defects (structural order–disorder) are responsible for the modifications of intermediary energy states within the band gap. These structural defects in the α-Ag$_2$WO$_4$ microcrystal lattice are responsible for the appearance of intermediate levels between the valence and conduction bands and favor the PL emission. In these energy states, after the photon absorption process, the recombination of electron–hole (e′–h$^\bullet$) pairs directly involves a CTB. Therefore, these structural defects promote a symmetry break, causing a polarization in the structure by the electronic charge transfer from ordered (o) to disordered (d) polyhedra (formation of e′–h$^\bullet$ pairs).[55] This phenomenon can be explained by eqn (9)–(13). In these equations, the superscript x indicates neutral polyhedra, $^\bullet$ the polyhedra with one hole – positive charge (h$^\bullet$), and ′ the polyhedra with one electron – negative charge (e′).

$$[AgO_n]_d^x + [AgO_n]_o^x \rightarrow [AgO_n]_d^\bullet + [AgO_n]_o' \qquad (9)$$

$$[WO_6]_d^x + [WO_6]_o^x \rightarrow [WO_6]_d^\bullet + [WO_6]_o' \qquad (10)$$

$$[AgO_n]_o^x + [EuO_y]_d^\bullet \rightarrow [EuO_n]_d^\bullet + [AgO_y]_d^x \qquad (11)$$

$$[AgO_n]_o' + [EuO_y]_d^\bullet \rightarrow [AgO_n]_o^x + [EuO_y]_d^x \qquad (12)$$

$$[WO_6]_o' + [EuO_y]_d^\bullet \rightarrow [WO_6]_d^x + [EuO_y]_d^x \qquad (13)$$

$n = 2$, 4, 6 and/or 7 and $y = 1$

Eqn (9) shows formation of e′–h$^\bullet$ pairs in the α-Ag$_2$WO$_4$ lattice due to the interaction of ordered [AgO$_n$]$_o^x$ and disordered

[AgO$_n$]$_d^x$ polyhedra (neutral polyhedra). The same interaction occurs in the ordered [WO$_6$]$_o^x$ and disordered [WO$_6$]$_d^x$ polyhedra as shown in eqn (10). Eqn (11) shows the influence that Eu^{3+} ions have on the polyhedron interaction process. PL suppression occurs in eqn (12), in which the [AgO$_n$]$_o'$ polyhedra (donor) transfer their electrons to [EuO$_y$]$_d^{\cdot}$ polyhedra (acceptor), resulting in neutral polyhedra. PL intensity also decreases due to the interaction involving [WO$_6$]$_o'$ and [EuO$_y$]$_d^{\cdot}$ polyhedra, which results in an electronic transfer from one polyhedra to another as shown in eqn (13). As e'–h$^{\cdot}$ pairs are not formed in eqn (11)–(13), the PL intensity decreases, which confirms Eu^{3+} ions as a matrix PL suppressor.

For Eu-doped samples, the blue-green emission is gradually quenched, and the narrow lines ascribed to Eu^{3+} emission are intensified. Probably, this behavior is accompanied by an increase in the intermediary energy levels within the band gap, as indicated by the decrease in the band gap values. It is possible to see a series of well-defined and narrow characteristic f–f transitions of Eu^{3+}, which confirms tungstate as an efficient host which can sensitize europium red emissions. It can be proved because the absorption cross section of rare earth ions is small due to the parity forbidden f–f transitions, which means that Eu^{3+} cannot be efficiently excited by the wavelength used. So, this host material seems to possess a higher absorption coefficient which not only holds the Eu^{3+} ions tightly but also leads to an efficient energy transfer to this ion. The spectra show four main emission bands peaking at 587 nm, 619 nm, 652 nm and 697 nm, assigned to $^5D_0 \rightarrow {}^7F_J$ (J = 1–4) transitions, respectively.

The energy level diagram of α-Ag$_{2-3x}$Eu$_x$WO$_4$ (x = 0, 0.0025, 0.005, 0.0075 and 0.01 mol) samples and possible energy transfer processes are schematically represented in Fig. 7. Upon 350.7 nm excitation, α-Ag$_{2-3x}$Eu$_x$WO$_4$ is excited from the ground to the excited state. Because the excited state of α-Ag$_{2-3x}$Eu$_x$WO$_4$ and the $^5L_6$ level of Eu^{3+} ions are energetically

Fig. 8 Excitation spectra of the α-Ag$_{2-3x}$Eu$_x$WO$_4$ synthesized by the coprecipitation method at 90 °C for 30 minutes. (a) x = 0.0025, (b) x = 0.005, (c) x = 0.0075 and (d) x = 0.01.

close to each other, energy transfer from α-Ag$_{2-3x}$Eu$_x$WO$_4$ to Eu^{3+} ions occurred. An excited state of α-Ag$_{2-3x}$Eu$_x$WO$_4$ relaxes from the excited to the ground state radiatively emitting in the blue region and nonradiatively transfers the excitation energy (ET) to a neighboring Eu^{3+} ion, promoting it from the $^7F_0$ ground state to the $^5L_6$ level. Finally, Eu^{3+} ions in the populated $^5L_6$ level undergo multi-phonon relaxation to the luminescent $^5D_0$ level that radiatively relax to ^7F_J (J = 1–4) levels, resulting in the characteristic emissions of Eu^{3+} ions.

Fig. 8 shows the excitation spectra recorded in the 270–500 nm range with the emission monitored at 616 nm (the hypersensitive $^5D_0 \rightarrow {}^7F_2$ transition of Eu^{3+}).

These spectra consist of one broad band around 270 nm and several sharp peaks in the 300–550 nm region. The former results from the charge transfer band (CTB) and may have different contributions. One of them is due to energy transfer between the Eu^{3+} ions and the surrounding oxygen anions (O^{2-}–Eu^{3+}). There is also charge (electron) transfer from the O^{2-} ligand to the W^{6+} ions in WO$_4{}^{2-}$ groups of the host lattice, which is also evidenced in the UV-vis spectra (Fig. 5). Finally, the last contribution is due to intervalence charge transfer (IVCT) states as a consequence of electron transition from the ground 4f state of Eu^{3+} to W^{6+}.[30] The latter part of the spectra is related to f–f transitions of Eu^{3+} ions and presents seven main absorption bands peaking at 306 nm, 382 nm, 393 nm, 414 nm, 464 nm, 524 nm and 532 nm, assigned to $^7F_0 \rightarrow {}^5H_3$, $^7F_0 \rightarrow {}^5L_7$, $^7F_0 \rightarrow {}^5L_6$, $^7F_0 \rightarrow {}^5D_3$, $^7F_0 \rightarrow {}^5D_2$ and $^7F_0 \rightarrow {}^5D_1$, transitions, respectively. The position of the bands and the corresponding bandwidths do not change with increasing concentration, indicating that the dopants are homogeneously distributed in the matrix.

Furthermore, it is important to notice that all samples can strongly absorb not only in the short (~270 nm) and lower (393 nm) UV ranges, but also in the visible (464, 524 and 532 nm) energy range. The main peaks located at around 393 and 464 nm, correspond to $^7F_0 \rightarrow {}^5L_6$ and $^7F_0 \rightarrow {}^5D_2$ transitions of Eu^{3+}, respectively. These two excitation peaks agree well with the characteristic emission from the commercially available near-UV and blue LED chips.[29]
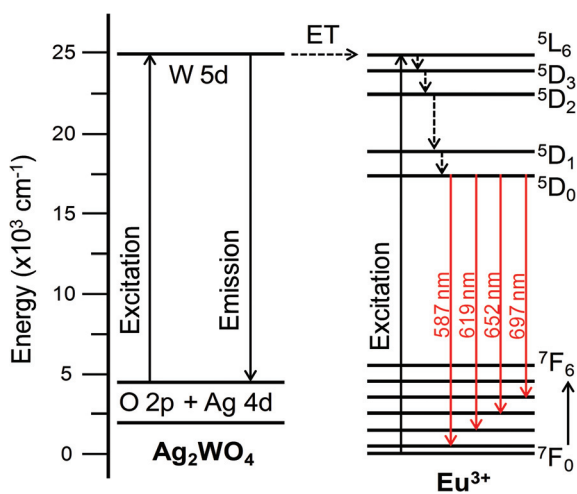

Fig. 7 Energy level diagram and proposed energy transfer mechanisms under 350.7 nm laser excitation in α-Ag$_{2-3x}$Eu$_x$WO$_4$ samples.
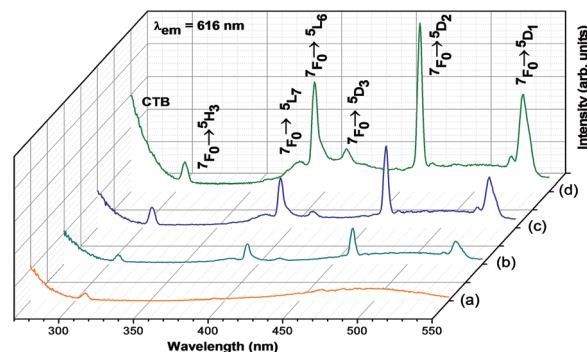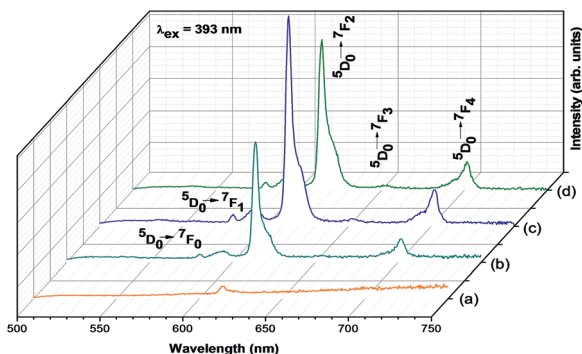
Fig. 9 Emission spectra of the α-Ag$_{2-3x}$Eu$_x$WO$_4$ synthesized by the coprecipitation method at 90 °C for 30 minutes. (a) x = 0.0025, (b) x = 0.005, (c) x = 0.0075 and (d) x = 0.01.

The emission spectra recorded in the 500–750 nm range with the excitation at 393 nm ($^7F_0 \rightarrow {}^5L_6$ electric dipole transition of Eu^{3+}) are shown in Fig. 9. The spectra show five main emission bands peaking at 580 nm, 593 nm, 614 nm, 651 nm and 701 nm, assigned to $^5D_0 \rightarrow {}^7F_J$ (J = 0–4) transitions, respectively. No apparent changes of peak positions in emission spectra ascribing to Eu^{3+} ions were observed, because the 4f energy levels of Eu^{3+} are little affected by the crystal field due to the shielding effect of the 5s^2 5p^6 electrons.[56] When the powders are excited at 393 nm, only the characteristic transitions of the Eu^{3+} ions are present; the lines are thinner and more defined possibly because at 393 nm the excitation is directly of the $^5L_6$ level of the Eu^{3+} ion, as observed in the excitation spectra. It is also observed that there are no bands arising from the ^5D_J (J = 1–3) emitting levels because the low-lying charge-transfer states skips the higher-lying ^5D_J levels during the relaxation process.

The characteristic emission peaks of Eu^{3+} transition at $^5D_0 \rightarrow {}^7F_1$ and $^5D_0 \rightarrow {}^7F_3$ are due to forced magnetic dipole transitions, while the transitions at $^5D_0 \rightarrow {}^7F_2$ and $^5D_0 \rightarrow {}^7F_4$ are due to forced electric dipole transitions. According to Judd–Ofelt theory, magnetic dipole transition is permitted and the electric dipole transition is only allowed when an ion occupies a site without an inversion center. Also, the electric dipole transition $^5D_0 \rightarrow {}^7F_2$ is sensitive to local symmetry and is more intense (hypersensitive) while the $^5D_0 \rightarrow {}^7F_1$ is little affected by the environment. Once $^5D_0 \rightarrow {}^7F_2$ (electric dipole) transition is more intense than $^5D_0 \rightarrow {}^7F_1$ (magnetic dipole), it can be concluded that Eu^{3+} occupies a site that lacks inversion symmetry.[57–59]

Moreover, the area ratio of $^5D_0 \rightarrow {}^7F_2$ and $^5D_0 \rightarrow {}^7F_1$ transitions gives valuable information about the local symmetry of Eu^{3+}. The relative area of ($^5D_0 \rightarrow {}^7F_2$)/($^5D_0 \rightarrow {}^7F_1$) transitions for all α-Ag$_{2-3x}$Eu$_x$WO$_4$ samples were calculated and the values obtained are 15.5, 25.9, 35.1 and 26.4 for x = 0.0025, x = 0.005, x = 0.0075 and x = 0.01, respectively. These results indicate that Eu^{3+} ions occupy sites having a less symmetry to the host matrix with an increased concentration since the relative area of ($^5D_0 \rightarrow {}^7F_2$)/($^5D_0 \rightarrow {}^7F_1$) transitions increases in all cases,

with an exception to α-Ag$_{2-3x}$Eu$_x$WO$_4$ (x = 0.01) sample where PL intensity decreases because of quenching. The presence of a band at 580 nm ($^5D_0 \rightarrow {}^7F_0$ transition) indicates that the Eu^{3+} ions should occupy sites of symmetry of the type C_s, C_n or C_{nv}. It suggests that one of the polyhedra that Eu^{3+} is localized is AgO$_2$ (C_{2v} site symmetry). In addition, if Eu^{3+} is in a site with inversion symmetry, the optical transitions inside the 4f^6 configuration are strictly forbidden as electric dipole transition. As a result, Eu^{3+} ions are not located in a site with inversion symmetry in the α-Ag$_2$WO$_4$ sample.[27]

The punctual groups for AgO$_n$ (n = 2, 4, 6 and 7) are C_{2v}, T_d, O_h and D_{5h}, respectively, and for WO$_6$ is O_h. Once the O_h punctual group has a center of inversion, we can assume that Eu^{3+} occupies Ag$^+$ sites of the polyhedra AgO$_n$ (n = 2, 4 and 7), which corroborate with XRD analyses.[30]

As Eu^{3+} doping concentration increased, enhancement of the photoluminescence intensity was observed up to 0.0075 mol and then decreases. So, when x = 0.0075, self-quenching concentration into the host matrix is observed. For x values of x = 0.0025 and x = 0.005, the lower doping concentration causes weak luminescence. This phenomenon appears because of nearest neighboring excited ions and the rise in the number of non-radiative decays. Actually, interaction between the Eu^{3+} ions causes energy loss by cross-relaxation. Energy transfer processes between the excited and unexcited Eu^{3+} ions were caused by a decrease in the number of optically active Eu^{3+} ions. Once all the spectra were recorded at room temperature, it is not possible to affirm if the quenching observed was because of thermal phonons. So, the optimum concentration for this matrix is 0.0075 mol.[27]

Fig. 10 depicts the PL decay curves of the $^5D_0 \rightarrow {}^7F_2$ transition for Eu^{3+} in the α-Ag$_{2-3x}$Eu$_x$WO$_4$ powders using emission and excitation wavelengths fixed at 614 and 393 nm, respectively. The decay curves are well fitted through a second order exponential decay as shown in eqn (14):

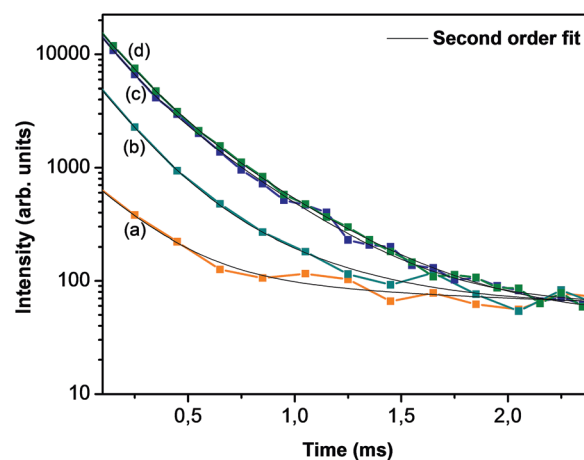$$I(t) = I_0 + \alpha_1 e^{(-t/\tau_1)} + \alpha_2 e^{(-t/\tau_2)} \tag{14}$$

Fig. 10 PL decays curves of the Eu^{3+} emission of the α-Ag$_{2-3x}$Eu$_x$WO$_4$ synthesized by the coprecipitation method at 90 °C for 30 minutes. (a) x = 0.0025, (b) x = 0.005, (c) x = 0.0075 and (d) x = 0.01.

Table 2 Lifetime, amplitude and average lifetime of the PL decay curves for α-Ag$_{2-3x}$Eu$_x$WO$_4$ synthesized by the coprecipitation method at 90 °C for 30 minutes

α-Ag$_{2-3x}$Eu$_x$WO$_4$	Lifetime (ms)			Amplitude	
	τ_1	τ_2	τ	α_1	α_2
x = 0.0025	0.24	1.66	0.77	768	66
x = 0.005	0.17	0.44	0.25	6950	1086
x = 0.0075	0.14	0.33	0.24	16 172	8203
x = 0.01	0.38	0.16	0.25	5879	19 576

where α_1 and α_2 represent the pre-exponential factor (amplitude) and τ_1 and τ_2 are the corresponding decay times ($R^2 \sim 0.999$). The average lifetime (τ), which is proportional to the total area under the fluorescence decay curve, is defined by eqn (15).

$$\tau = \frac{\sum_i \alpha_i \tau_i^2}{\sum_i \alpha_i \tau_i} \quad (15)$$

The amplitudes, decay times and average lifetime values are shown in Table 2. Once the profiles of the curves are fitted by this equation, it indicates that two processes govern the luminescence. It is possible to observe a tendency for monoexponential behavior as the Eu^{3+} concentration is increased. This is an indication that the coordination environment of the rare earth ions tends to become more homogeneous in the α-Ag$_2$WO$_4$ matrix.

CIE chromaticity

Measurement of color perceived by the human eye was evaluated by the *Commission internationale de léclairage* (CIE) chromaticity diagram. Luminescence color coordinates of α-Ag$_{2-3x}$Eu$_x$WO$_4$ (x = 0, 0.0025, 0.005, 0.0075 and 0.01 mol) crystals synthesized by the CP method at 90 °C for 30 minutes and excited at 350.7 nm are plotted in the CIE chromaticity diagram shown in Fig. 11.

Table 3 lists the chromaticity coordinates x and y for α-Ag$_{2-3x}$Eu$_x$WO$_4$ (x = 0, 0.0025, 0.005, 0.0075 and 0.01 mol) crystals. When Eu^{3+} is absent, a broad band in the blue region and a less intense band of red contribution due to AgO$_n$ (n = 2, 4, 6 and 7) polyhedra is observed, which results in a purplish pink color (Fig. 11(a)). Addition of just 0.0025 mol of Eu^{3+} ions is sufficient to result in a pale pink color due to the sum of both blue and intense red emissions (Fig. 11(b)). When the Eu^{3+} content reaches 0.005 mol, a pale orange color is obtained because the blue emission begins to disappear and the Eu^{3+} peaks increase in intensity (Fig. 11(c)).

When 0.0075 mol of Eu^{3+} was used, a more pronounced orange color appears because the blue emission is almost negligible (Fig. 11(d)). For 0.01 mol of Eu^{3+}, an intense pink color appears because the intense f–f emission from Eu^{3+} dominates over the WO$_4^{2-}$ blue emission (Fig. 11(e)).

Fig. SI2† shows the CIE diagram coordinates of the α-Ag$_{2-3x}$Eu$_x$WO$_4$ synthesized by the CP method at 90 °C for

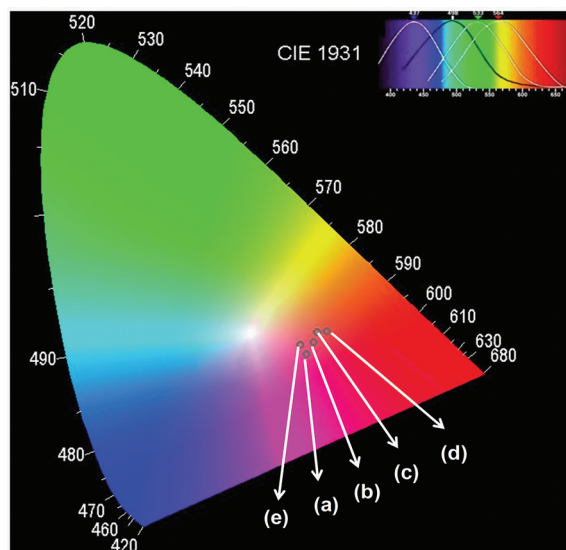**Fig. 11** CIE diagram coordinates of the α-Ag$_{2-3x}$Eu$_x$WO$_4$ synthesized by the coprecipitation method at 90 °C for 30 minutes. (a) x = 0, (b) x = 0.0025, (c) x = 0.005, (d) x = 0.0075 and (e) x = 0.01.

Table 3 Chromatic coordinates x and y for α-Ag$_{2-3x}$Eu$_x$WO$_4$ (x = 0, 0.0025, 0.005, 0.0075 and 0.01 mol) synthesized by the coprecipitation method at 90 °C for 30 minutes

α-Ag$_{2-3x}$Eu$_x$WO$_4$	Chromatic coordinate	
	x	y
x = 0	0.440	0.298
x = 0.0025	0.452	0.318
x = 0.005	0.459	0.336
x = 0.0075	0.474	0.337
x = 0.01	0.430	0.314

30 minutes, using a Xe lamp as an excitation source. Table SI4† shows the corresponding chromatic coordinates x and y for these samples. The results show that all samples have predominantly the orange-red color because there is no matrix PL band when using the Xe lamp as the source. So, just the bands corresponding to the f–f transition of Eu^{3+} contributes to the color of the material.

For rare earth doped materials, emission color output can be tuned through different types and levels of doping ions, introduction of non-rare earth ions, new host, experimental conditions, particle size, crystallinity and phase.[23]

In this work, small amounts of only one rare earth were enough to tune different colors due to the combination of intrinsic visible luminescence of tungstate in the blue region and the characteristic luminescence of Eu^{3+} in the red region. These results confirm that these materials are suitable for application in several visible lamps, displays and other optical devices.
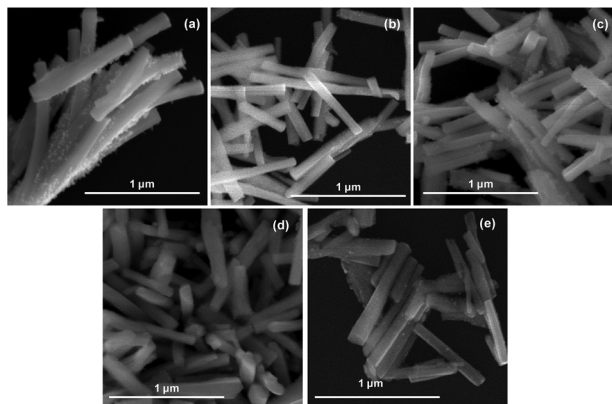
Fig. 12 FE-SEM images of the α-Ag$_{2-3x}$Eu$_x$WO$_4$ synthesized by the coprecipitation method at 90 °C for 30 minutes. (a) $x = 0$, (b) $x = 0.0025$, (c) $x = 0.005$, (d) $x = 0.0075$ and (e) $x = 0.01$.

Morphological analysis

Scanning Electron Microscopy was used to evaluate particle size, homogeneity and shape of the crystals. In the field of optoelectronics it is important to consider the morphology of the materials for efficient application in nanodevices. One dimensional (1D) structures such as rods, tubes and belts are practical examples with unique properties for this purpose.[60]

Fig. 12 shows the FE-SEM images of α-Ag$_{2-3x}$Eu$_x$WO$_4$ ($x = 0$, 0.0025, 0.005, 0.0075 and 0.01 mol) crystals obtained by the CP method at 90 °C for 30 minutes. Fig. 12(a) depicts hexagonal nanorod-like α-Ag$_{2-3x}$Eu$_x$WO$_4$ ($x = 0$) crystals with an average length of around 1 μm and a diameter of around 50 nm. The image shows uniformly size distributed and agglomerated nature through lateral hexagonal nanorod-like shape elongated in the y-axis along the [010] direction.[61] This indicates the formation of nanorod morphology for the α-Ag$_2$WO$_4$. Increasing temperature favors the increase of diameter of 1D structure, but the synthesis was carried out by maintaining the temperature at 90 °C, so this factor did not influence the sample sizes.[33] The small structures on the superficial of nanorods are related to Ag growing and were well explained previously by our research group.[18]

Fig. 12(b)–(e) shows the α-Ag$_{2-3x}$Eu$_x$WO$_4$ ($x = 0.0025$, 0.005, 0.0075 and 0.01 mol) crystals. Overall, the typical shape of the samples was the same once the content of europium was small to promote changes in the shape of nanorods. Moreover, it was verified that the agglomerate nature still persists in this system. However, Fig. 12(e) shows that the incorporation of 0.01 mol of Eu^{3+} into the lattice promoted the reduction of length and maintenance of diameter for some nanocrystals. At the moment, we cannot affirm any influence that Eu^{3+} has on Ag growing process. Regular 1-D nanorods of mean size of 1 μm in width were achieved without any kind of template, capping agent, surfactant or catalyst as a result of favorable conditions of the CP methodology.[32]

A semi-quantitative analysis of the powders obtained was performed using the EDS data. Fig. SI3† shows the EDS spectra of α-Ag$_{2-3x}$Eu$_x$WO$_4$ ($x = 0$, 0.0025, 0.005, 0.0075 and 0.01 mol) crystals obtained by the CP method at 90 °C for 30 minutes. The results clearly indicate that the samples are composed of Ag ($K_\alpha = 23.173$ eV, $L_\alpha = 3.133$ eV), W ($L_\alpha = 8.398$ eV, $M_\alpha = 1.775$ eV) and O ($K_\alpha = 0.525$ eV) since their peaks were observed as expected. The presence of the Eu ($L_\alpha = 5.849$ eV, $M_\alpha = 1.131$ eV) peak was also observed and the content was estimated in 0.33, 0.48, 0.94 and 1.33 wt% for α-Ag$_{2-3x}$Eu$_x$WO$_4$ ($x = 0.0025$, 0.005, 0.0075 and 0.01 mol) samples, respectively. These values are close to the theoretically calculated values.

Conclusion

Functional europium doped silver tungstates were synthesized effectively by the coprecipitation methodology using low temperatures and a short annealing time. The Eu^{3+} content used here was introduced into the silver tungstate lattice with no undesirable phase segregation. XRD and Rietveld refinement revealed that α-Ag$_{2-3x}$Eu$_x$WO$_4$ nanocrystal samples are ordered at a long range. MR and FT-IR analysis revealed more defined bands with the increase in Eu^{3+} content, which indicate structural order at a short range due to the insertion of this rare earth ion. UV-vis showed that the Eu^{3+} content was sufficient to create new energy levels within the band gap. FE-SEM revealed hexagonal nanorods for all crystals with a size of about 1 μm. The silver tungstate acted as a rigid host lattice which provides a steady microenvironment for Eu^{3+} emitter as could be seen from the PL spectra. PL spectroscopy and lifetime decay also suggested that Eu^{3+} ions are located in at least two of the AgO$_n$ ($n = 2$, 4 or 7) polyhedra. The CIE chromaticity coordinates showed different tones of pink for the samples. Moreover, these results confirm these materials as good candidates for use in phosphors in the visible range of electromagnetic spectra.

Acknowledgements

References

1 A. K. Vishwakarma, K. Jha, M. Jayasimhadri, A. S. Rao, K. Jang, B. Sivaiah and D. Haranath, *J. Alloys Compd.*, 2015, **622**, 97–101.

2 Y. Zhang, H. Jiao and Y. Du, *J. Lumin.*, 2011, **131**, 861–865.

3 M. Galceran, M. C. Pujol, P. Gluchowski, W. Stręk, J. J. Carvajal, X. Mateos, M. Aguiló and F. Díaz, *Opt. Mater.*, 2010, **32**, 1493–1500.

4   Q.-W. Song, B. Yu, X.-D. Li, R. Ma, Z.-F. Diao, R.-G. Li, W. Li and L.-N. He, *Green Chem.*, 2014, **16**, 1633.

5   C.-X. Guo, B. Yu, J.-N. Xie and L.-N. He, *Green Chem.*, 2014, **17**, 474–479.

6   V. M. Longo, C. C. De Foggi, M. M. Ferrer, A. F. Gouveia, R. S. Andre, W. Avansi, C. E. Vergani, A. L. Machado, J. Andres, L. S. Cavalcante, A. C. Hernandes and E. Longo, *J. Phys. Chem. A*, 2014, **118**, 5769–5778.

7   L. Cheng, Q. Shao, M. Shao, X. Wei and Z. Wu, *J. Phys. Chem. C*, 2009, **113**, 1764–1768.

8   L. S. Cavalcante, M. A. Almeida, W. Avansi Jr., R. L. Tranquilin, E. Longo, N. C. Batista, V. R. Mastelaro and M. S. Li, *Inorg. Chem.*, 2012, **51**, 10675–10687.

9   R. Zhang, H. Cui, X. Yang, H. Liu, H. Tang and Y. Li, *Micro Nano Lett.*, 2012, **7**, 1285–1288.

10 X. Liu, J. Hu, J. Li, Y. Hu, Y. Shao, H. Yang, G. Tong and H. Qian, *Mater. Lett.*, 2013, **91**, 129–132.

11 H. Chen and Y. Xu, *Appl. Surf. Sci.*, 2014, **319**, 319–323.

12 J. Tang and J. Ye, *J. Mater. Chem.*, 2005, **15**, 4246.

13 X. Wang, C. Fu, P. Wang, H. Yu and J. Yu, *Nanotechnology*, 2013, **24**, 165602.

14 D. Stone, J. Liu, D. P. Singh, C. Muratore, A. A. Voevodin, S. Mishra, C. Rebholz, Q. Ge and S. M. Aouadi, *Scr. Mater.*, 2010, **62**, 735–738.

15 L. Pan, L. Li and Y. Chen, *J. Sol-Gel Sci. Technol.*, 2013, **66**, 330–336.

16 L. F. da Silva, A. C. Catto, W. Avansi Jr., L. S. Cavalcante, J. Andres, K. Aguir, V. R. Mastelaro and E. Longo, *Nanoscale*, 2014, **6**, 4058–4062.

17 Q. Wang, X. Guo, W. Wu and S. Liu, *Adv. Mater. Res.*, 2011, **284–286**, 1321–1325.

18 E. Longo, L. S. Cavalcante, D. P. Volanti, A. F. Gouveia, V. M. Longo, J. A. Varela, M. O. Orlandi and J. Andres, *Sci. Rep.*, 2013, **3**, 1–4.

19 E. Longo, D. P. Volanti, V. M. Longo, L. Gracia, I. C. Nogueira, M. A. P. Almeida, A. N. Pinheiro, M. M. Ferrer, L. S. Cavalcante and J. Andrés, *J. Phys. Chem. C*, 2014, **118**, 1229–1239.

20 J. Andres, L. Gracia, P. Gonzalez-Navarrete, V. M. Longo, W. Avansi Jr., D. P. Volanti, M. M. Ferrer, P. S. Lemos, F. A. La Porta, A. C. Hernandes and E. Longo, *Sci. Rep.*, 2014, **4**, 1–7.

21 W. D. Pereira, J. Andres, L. Gracia, M. A. San-Miguel, E. Z. da Silva, E. Longo and V. M. Longo, *Phys. Chem. Chem. Phys.*, 2015, **17**, 5352–5359.

22 X.-Y. Zhang, J.-D. Wang, J.-K. Liu, X.-H. Yang and Y. Lu, *CrystEngComm*, 2015, **17**, 1129–1138.

23 S. Gai, C. Li, P. Yang and J. Lin, *Chem. Rev.*, 2014, **114**, 2343–2389.

24 X. Wang, B. Liu and Y. Yang, *Opt. Laser Technol.*, 2014, **58**, 84–88.

25 V. Lisitsyn, D. Valiev, I. Tupitsyna, E. Polisadova, L. Lisitsyna, L. Andryuschenko, A. Dubovik, A. Yakubovskaya and O. Vovk, *Adv. Mater. Res.*, 2014, **872**, 128–133.

26 C. A. Kodaira, H. F. Brito and M. C. F. C. Felinto, *J. Solid State Chem.*, 2003, **171**, 401–407.

27 K. Gayatri Sharma, N. Shanta Singh, Y. Rangeela Devi, N. Rajmuhon Singh and S. Dorendrajit Singh, *J. Alloys Compd.*, 2013, **556**, 94–101.

28 P. F. S. Pereira, A. P. de Moura, I. C. Nogueira, M. V. S. Lima, E. Longo, P. C. de Sousa Filho, O. A. Serra, E. J. Nassar and I. L. V. Rosa, *J. Alloys Compd.*, 2012, **526**, 11–21.

29 F.-W. Kang, Y.-H. Hu, L. Chen, X.-J. Wang, H.-Y. Wu and Z.-F. Mu, *J. Lumin.*, 2013, **135**, 113–119.

30 P. S. Dutta and A. Khanna, *ECS J. Solid State Sci. Technol.*, 2013, **2**, R3153–R3167.

31 F. Lei and B. Yan, *J. Mater. Res.*, 2011, **26**, 88–95.

32 S.-H. Yu, B. Liu, M.-S. Mo, J.-H. Huang, X.-M. Liu and Y.-T. Qian, *Adv. Funct. Mater.*, 2003, **13**, 639–647.

33 X. Cui, S. H. Yu, L. Li, L. Biao, H. Li, M. Mo and X. M. Liu, *Chem. – Eur. J.*, 2004, **10**, 218–223.

34 T. George, S. Joseph and S. Mathew, *Pramana – J. Phys.*, 2005, **65**, 793–799.

35 J. S. McKechnie, L. D. S. Turner and C. A. Vincent, *J. Radioanal. Nucl. Chem.*, 1979, **41**, 177–179.

36 A. C. Larson and R. B. V. Dreele, *Journal*, 2004.

37 P. M. Skarstad and S. Geller, *Mater. Res. Bull.*, 1975, **10**, 791–799.

38 P. V. Korake, A. N. Kadam and K. M. Garadkar, *J. Rare Earths*, 2014, **32**, 306–313.

39 Y. Zheng, J. Lin and Q. Wang, *Photochem. Photobiol. Sci.*, 2012, **11**, 1567–1574.

40 H. M. Rietveld, *J. Appl. Crystallogr.*, 1969, **2**, 65–71.

41 D. E. C. P. Thompson and J. B. Hastings, *J. Appl. Crystallogr.*, 1987, **20**, 79–83.

42 L. W. Finger, D. E. Cox and P. Jephcoat, *J. Appl. Crystallogr.*, 1994, **27**, 892–900.

43 P. W. Stephens, *J. Appl. Crystallogr.*, 1999, **32**, 281–289.

44 K. Momma and F. Izumi, *J. Appl. Crystallogr.*, 2011, **44**, 1272–1276.

45 T. T. Basiev, A. A. Sobol, Y. K. Voronko and P. G. Zverev, *Opt. Mater.*, 2000, **15**, 205–216.

46 A. Turkovic, D. L. Fox and J. F. Scott, *Mater. Res. Bull.*, 1977, **12**, 189–196.

47 T. M. Mazzo, L. Mendonça da Rocha Oliveira, L. R. Macario, W. Avansi, R. D. Silveira André, I. L. Viana Rosa, J. A. Varela and E. Longo, *Mater. Chem. Phys.*, 2014, **145**, 141–150.

48 F. Shi, J. Meng, Y. Ren and Q. Su, *J. Phys. Chem. Solids*, 1998, **59**, 105–110.

49 G. M. Clark and W. P. Doyle, *Spectrochim. Acta*, 1966, **22**, 1441–1447.

50 P. Kubelka and F. Munk, *Zeit. Für. Tech. Physik.*, 1931, **12**, 593.

51 M. L. Myrick, M. N. Simcock, M. Baranowski, H. Brooke, S. L. Morgan and J. N. McCutcheon, *Appl. Spectrosc. Rev.*, 2011, **46**, 140–165.

52 D. Wood and J. Tauc, *Phys. Rev. B: Solid State*, 1972, **5**, 3144–3151.

53 D. W. Kim, I.-S. Cho, S. Lee, S.-T. Bae, S. S. Shin, G. S. Han, H. S. Jung and K. S. Hong, *J. Am. Ceram. Soc.*, 2010, **93**, 3867–3872.

54 F. A. Kröger and H. J. Vink, *Solid State Phys.*, 1956, **3**, 307–435.

55 G. Botelho, J. C. Sczancoski, J. Andres, L. Gracia and E. Longo, *J. Phys. Chem. C*, 2015, **119**, 6293–6306.

56 J. Wang, Z.-J. Zhang, J.-T. Zhao, H.-H. Chen, X.-X. Yang, Y. Tao and Y. Huang, *J. Mater. Chem.*, 2010, **20**, 10894–10900.

57 R. F. Gonçalves, L. S. Cavalcante, I. C. Nogueira, E. Longo, M. J. Godinho, J. C. Sczancoski, V. R. Mastelaro, I. M. Pinatti, I. L. V. Rosa and A. P. A. Marques, *CrystEngComm*, 2015, **17**, 1654–1666.

58 T. M. Mazzo, I. M. Pinatti, L. R. Macario, W. Avansi Junior, M. L. Moreira, I. L. V. Rosa, V. R. Mastelaro, J. A. Varela and E. Longo, *J. Alloys Compd.*, 2014, **585**, 154–162.

59 F. Lei, B. Yan, H. H. Chen and J. T. Zhao, *J. Am. Ceram. Soc.*, 2009, **92**, 1262–1267.

60 Y. Zheng, X. Lin, Q. Wang, W. Cai and C. C. Zhang, *Mater. Res. Bull.*, 2012, **47**, 856–860.

61 R. A. Roca, J. C. Sczancoski, I. C. Nogueira, M. T. Fabbro, H. C. Alves, L. Gracia, L. P. S. Santos, C. P. d. Sousa, G. E. D. L. Júnior, J. Andres, E. Longo and L. S. Cavalcante, *Catal. Sci. Technol.*, 2015, **5**, 4091–4107.